A numerical parametric study of the mechanical action of pulsatile blood flow onto axisymmetric stenosed arteries

Tristan Belzacq, Stéphane Avril, Emmanuel Leriche, Alexandre Delache

A numerical parametric study of the mechanical action of pulsatile blood flow onto axisymmetric stenosed arteries

Tristan Belzacq*†, Stéphane Avril† Emmanuel Leriche and Alexandre Delache‡

***Corresponding author**

Email: belzacq@emse.fr

†Ecole Nationale Supérieure des Mines, Centre Ingénierie et Santé, CNRS UMR 5146, 158 cours Fauriel, 42023 Saint-Etienne cedex 2, France

Laboratoire de Mécanique de Lille, Université de Lille, Avenue Paul Langevin, Cité Scientifique, F-59655 Villeneuve d'Ascq cedex, France

‡ Laboratoire de Mécanique des fluides et d'acoustique LMFA, site de St-Etienne, Université de Lyon, F-42023 St-Etienne, France, Université Jean Monnet de St-Etienne, Faculté des Sciences et Techniques, 23 rue du Docteur Paul Michelon, 42023 St-Etienne cedex 2, France

Abstract

In the present paper, a fluid structure interaction model is developed, questioning how the mechanical action of the blood onto an atheromatous plaque is affected by the length and the severity of the stenosis. An axisymmetric model is considered. The fluid is assumed Newtonian. The plaque is modelled as a heterogeneous hyperelastic anisotropic solid composed of the arterial wall, the lipid core and the fibrous cap. Transient velocity and pressure conditions of actual pulsatile blood flow are prescribed. The simulation is achieved using the Arbitrary Lagrangian Eulerian scheme in the COMSOL commercial Finite Element package. The results reveal different types of behaviour in function of the length (denoted L) and severity (denoted S) of the stenosis. Whereas large plaques (L>10mm) are mostly deformed under the action of the blood pressure, it appears that shorter plaques (L<10mm) are significantly affected by the shear stresses. The shear stresses tend to deform the plaque by pinching it. This effect is called: "the pinching effect". It has an essential influence on the mechanical response of the plaque. For two plaques having the same radius severity S=45%, the maximum stress in the fibrous cap is 50% larger for the short plaque (L=5mm) than for a larger plaque (L=10mm), and the maximum wall shear stress is increased of 100%. Provided that they are confirmed by experimental investigations, these results may offer some new perspectives for understanding the vulnerability of short plaques.

Keywords*:* vascular biomechanics; fluid structure interaction; numerical simulation; stenosis; blood flow

Global variables:

ρ the density

η the viscosity

R_0 the healthy arterial radius

h_0 the thickness of the healthy arterial wall

e the fibrous cap thickness

L the stenosis length

R_m the external stenosis remodelling radius

S the stenosis severity in terms of diameter

S_{area} the stenosis severity in terms of area

$(\alpha_k)_k$ the series of Womersley number

$\mathbf{e}_z$ the longitudinal axis in the cylindrical frame

$\mathbf{e}_r$ the radial axis in the cylindrical frame

n exterior normal

u the displacement vector

v the velocity

p the pressure

σ the stress tensor

F the deformation gradient tensor

C the Green-Cauchy right strain tensor

φ the strain energy density

J the volume change invariant

I_1, I_4 and I_6 the first, fourth and sixth coordinate invariants

c, k_1 and k_2 the parameters of the Holzapfel model

β the angle between these two fibres family

M and **M**' the direction's vectors of the two fiber's family in the cylindrical coordinate

w the mesh velocity in the Arbitrary Lagrangian Eulerian scheme

τ the wall shear stress

ε_R the average radial strain of the plaque

γ the average shear strain of the plaque

U_r the radial displacement component of the fibrous cap at the middle of the stenosis

U_z the longitudinal displacement of the fibrous cap at the middle of the stenosis

P_1 the linear type of finite elements

P_2 the quadratic type of finite elements

Ω a domain

$\partial\Omega$ a boundary

Indexes:

s the solid part

f the fluid part

fs fluid-structure

i the material number ($1 \le i \le 4$)

in inlet

out outlet
ext exterior
sym symmetric
max maximum

Operators:

det(.) the determinant of a tensor
$\frac{\partial .}{\partial t}$ the first derivative with respect to time
$\frac{\partial^2 .}{\partial t^2}$ the second derivative with respect to time
$\nabla .$ the divergence operator
∇ the gradient operator
I the identity matrix
$^t\mathbf{A}$ transpose of the matrix **A**
Re(.) the real part of an imaginary number
$J_0(.)$ the zero order Bessel function of first kind

1. Introduction

The fracture of vulnerable carotid atherosclerotic plaques is the major cause of cerebrovascular thromboembolic events such as strokes and ischemic attacks [1]. The vulnerability is believed to be related to mechanical forces, vessel surface condition, cell activities and chemical environment [2-4].

In current clinical practice, carotid endarterectomy is the most frequently used treatment for pathological plaques. The decision leading to surgery is based on the degree of endoluminal stenosis [5,6]. But this criterion alone is insufficient to predict the plaque fracture and the necessity to identify other criteria is a major issue for public health [1]. Therefore, there is a strong medical and economical interest in developing new tools for a better understanding of this situation.

Histological studies have related plaque vulnerability with thin fibrous cap, large necrotic core [2] and inflammation after macrophages or T-cells infiltration in the lipid core [3] or foam cells infiltration in the fibrous cap [4]. Advanced magnetic resonance imaging (MRI) allows *in vivo* virtual histology of plaques [7,8].

There has also been considerable effort using computational models to perform mechanical analysis for atherosclerotic plaques and identify critical mechanical descriptors as stresses or strains related to plaque rupture. There is no universal technique that can measure the strain/stress field in the plaque but it is widely believed that stress concentration in the fibrous cap of vulnerable plaques can cause the rupture [9,10]. Large cyclic variations of strain/stress may also lead to artery fatigue [11-13]. Several studies, for example, indicate that the critical strain/stress conditions are affected by the stenosis severity, the lipid pool size, the fibrous cap thickness and the stenosis eccentricity [14-17].

2-D and 3-D patient-specific finite-element (FE) models of diseased vessels are probably the best way to obtain stress distributions for specific plaques. The models are based on histology or pre-fracture medical imaging [18]. Their purpose is to associate the mechanical descriptors to the mechanical process of plaque rupture.

Nevertheless the sparsity of data regarding plaque rupture reveals the limitations of the predictive models. The models may be:

- fluid models [19-21] with rigid plaques
- 2D solid models under pressure loads [14,22-26] considering cross sections of idealized plaques

- or fluid structure interaction (FSI) models taking into account both the combination of shear and pressure loads [9,10,18,27-33].

FSI models are probably the most realistic models but their models are complex. The interaction between the blood flow and the plaque is not yet fully understood, especially due to the large variability of plaques [8]. Using idealized models allows investigating how the mechanical action of the blood onto the plaque is affected by the geometry and the mechanical properties. For instance, Li Z.Y. et al. [15] studied the influence of stenosis severity and fibrous cap thickness on stresses in plaques with 2D plane-strain models. Li M.X. et al. [16] investigated the stress distribution for different degrees of stenoses also with 2D-axisymmetric models. Valencia et al. [34] investigated the influence of the severity of stenoses on stresses with 3D-axisymmetric models. Tang et al. performed many 3D FSI studies on idealized plaque models. They analysed wall stress and strain in symmetric and asymmetric plaque models with two different stenosis severities: 50% and 78% [17,35]. They analysed also the influence of pressure loads and stenosis severity on the cyclic compression of plaques [12,36].

The effect of plaque length has never been investigated in the literature. The present paper aims at addressing this lack. A FSI 2D axisymmetric model of the blood flow in a smooth pipe is considered, with a thick, deformable, heterogeneous and axisymmetric stenosis, mimicking an atherosclerotic plaque in a straight segment of artery. The model allows rapid modifications of the geometrical and constitutive parameters of the plaque for evaluating the influence of all these parameters.

2. Methods

2.1 Geometrical model

A schematic of the geometry in the reference configuration (i.e. in unloaded pressure-free conditions [32,37]) is provided in Fig. 1. The model of the plaque is axisymmetric (Fig. 1-D). The initial stenosis shape starts from a sinus shape function along the longitudinal direction. It is composed of the healthy arterial wall outside and of a fibrous cap containing the lipid core inside (Fig. 1-B).

The healthy arterial lumen has an inner radius of $R_0 = 3\,\text{mm}$ and a wall thickness of $h_0 = 0.5\,\text{mm}$ (Fig. 1-C), which corresponds to average values for the wall of the carotid artery [38].

Most of vulnerable carotid plaques present a positive remodelling [39] which is modelled as an external remodelling radius of the vessel. It is set here to $R_m = 1\text{mm}$ [39].

The reference for the plaque length is set to L=10mm. This value corresponds to the average length of carotid plaques [40]. The stenosis height H_0 is related to the stenosis severity, denoted S. Eq. 1 gives the expression of the stenosis severity as the ratio between the stenosis height and the healthy radius [5,6]. In the present study as in [5,6], the radius severity is considered. Clinicians sometimes consider the stenosis severity in terms of cross-sectional area reduction (denoted S_{area}). Eq. 2 gives the conversion formula between the radius severity and the area severity.

$$S = 1 - \frac{R_0\text{-}H_0\text{-}e}{R_0} \qquad (1)$$

$$S_{area} = 1 - (1 - S)^2 \qquad (2)$$

According to NASCET or ECST studies [5,6], a plaque is vulnerable if the stenosis radius severity is above 70%. However it is widely believed that this criterion alone is not sufficient to characterize the vulnerability of plaques [1]. The current study considers moderately severe plaques (reference value S=45%) and investigate the effect of other parameters on the vulnerability.

The fibrous cap thickness is a critical geometrical characteristic for plaque vulnerability because thrombo-embolic events result from the fibrous cap rupture. To place the study in a case of vulnerable plaque, a thin fibrous cap is considered (e=0.1mm) [15]. To simplify the idealized plaque model, the fibrous cap thickness is homogeneous along the stenosis.

The arterial length upstream stenosis is set to 20 mm. This is necessary for establishing the flow without having the influence of inflow boundary conditions prescribed at the inlet. For the same reason, the arterial length downstream the stenosis is set to 50 mm ensuring the establishment of the eventual flow recirculation.

2.2 Fluid and structural equations

A pulsatile flow of a viscous Newtonian and incompressible fluid is considered in an axisymmetric pipe (Fig. 1-A), with a pulsation $\omega = 2\pi$ [41]. This flow behaviour is suitable for simulating the flow in large arteries because Non-newtonian effects are believed to have a

minor influence (see discussion in section 4.3). Its dynamic viscosity is denoted η_f and the density of the fluid is denoted ρ_f. The fluid velocity field $\mathbf{v}_f$ and pressure field p are governed by the unsteady incompressible Navier-Stokes equations written in the Arbitrary Lagrangian-Eulerian (ALE) formulation [42]:

$$\begin{cases} \rho_f \dfrac{\partial \mathbf{v}_f}{\partial t} + \rho_f(\mathbf{v}_f - \mathbf{w}).\nabla \mathbf{v}_f - \nabla.\boldsymbol{\sigma}_f = \mathbf{0} \\ \nabla.\mathbf{v}_f = 0 \end{cases} \quad in \quad \Omega_f \quad , \qquad (3)$$

where $\mathbf{w}$ is the mesh velocity related to the ALE formulation, $\boldsymbol{\sigma}_f$ the Cauchy stress tensor in the fluid and Ω_f is the fluid domain depicted in Fig.1-A.

The displacement vector, denoted $\mathbf{u}_s$, and the Cauchy stress tensor, denoted $\boldsymbol{\sigma}_s$, of the solid part, with respect to the reference configuration, satisfy the following equation [43]:

$$\rho_s \frac{\partial^2 \mathbf{u}_s}{\partial t^2} - \nabla.\boldsymbol{\sigma}_s = \mathbf{0} \quad in \quad \Omega_s \, , \qquad (4)$$

where Ω_s is depicted in Fig.1-A and ρ_s is the density of the constituents in the solid domain, which is assumed homogeneous.

2.3 Fluid and structural boundary conditions

At the inlet of the fluid domain, a Womersley velocity profile [44] is applied and at the outlet, a pressure is imposed implying no normal viscous stress (see Eq. 5). The time variations of the pressure and the velocity profiles are written using Fourier decomposition, with 18 and 6 terms respectively for ensuring agreement with experimental data. Fourier decomposition is applied to the temporal signals shown in Fig. 2.

246
$$\begin{cases} \mathbf{v}_f(r,t) = -\frac{c_0}{4\eta_f}R^2(1-(\frac{r}{R})^2) - \frac{R^2}{\eta_f}\sum_{k=0}^{6}\mathrm{Re}(\frac{ic_k}{\alpha_k^2}(1-\frac{J_0(\alpha_k\frac{r}{R}i^{\frac{3}{2}})}{J_0(\alpha_k i^{\frac{3}{2}})})e^{ik\omega t})\mathbf{e}_z \quad on \quad \partial^{in}\Omega_f \\ p(t) = \sum_{k=0}^{18}\mathrm{Re}(p_k e^{ik\omega t}) \quad on \quad \partial^{out}\Omega_f \\ \boldsymbol{\sigma}_f^{viscous}\mathbf{e}_z = \mathbf{0} \quad on \quad \partial^{out}\Omega_f \end{cases}, \quad (5)$$

247 where $\partial^{in}\Omega_f$ and $\partial^{out}\Omega_f$ are respectively the inlet and the outlet boundaries of the fluid
248 depicted in Fig. 1-A, $\mathbf{e}_z$ is the longitudinal vector and J_0 is the zero order Bessel function of
249 first kind, *R* is the radius of the pipe at the inlet and $(\alpha_k = R\sqrt{\frac{k\omega\rho_f}{\eta_f}})_{0\le k\le 6}$ is the series of
250 Womersley numbers.
251
252 $\sigma_f^{viscous}$ represents the viscous stress part of the Cauchy stress tensor in the fluid σ_f (see Eq. 8
253 in the section 2.4).
254
255 The axial velocity at the inlet is represented in Fig. 2-A and the pressure at the outlet is
256 represented in Fig. 2-B [46].
257
258 The Fourier coefficients c_k (Tab. 3) of the Womersley profile are computed from the axial
259 velocity data measured non-invasively using PC-MRI in the common carotid artery of a
260 volunteer [46]. Moreover the pressure Fourier coefficients p_k (Tab. 3) are deduced from the
261 variations over cardiac cycles of the pressure measured non-invasively using the applanation
262 tonometry technique on the same volunteer [47].
263

At the boundaries of the elastic solid, the displacement vector $\mathbf{u}_s$ and the Cauchy stress tensor $\boldsymbol{\sigma}_s$, with respect to the reference configuration, satisfy the following equations [43]:

$$\begin{cases} \boldsymbol{\sigma}_s \mathbf{n}_{s,ext} = \mathbf{0} \quad on \quad \partial^{ext}\Omega_s \\ \mathbf{u}_s . \mathbf{e}_z = 0 \quad on \quad \partial^{in}\Omega_s \quad and \quad \partial^{out}\Omega_s \end{cases} , \qquad (6)$$

where $\partial^{ext}\Omega_s$, $\partial^{in}\Omega_s$, $\partial^{out}\Omega_s$ and the normal vector $\mathbf{n}_{s,ext}$ are depicted in Fig.1-A.

At the fluid-structure interface $\partial\Omega_{fs}$ (see Fig. 1-A), the kinematic and dynamic conditions apply, ensuring continuity of velocity fields and normal stresses:

$$\begin{cases} \mathbf{v}_f = \dfrac{\partial \mathbf{u}_s}{\partial t} = \mathbf{w} \\ \boldsymbol{\sigma}_s \mathbf{n}_s + \boldsymbol{\sigma}_f \mathbf{n}_f = \mathbf{0} \end{cases} \text{ on } \quad \partial\Omega_{fs} \qquad , \qquad (7)$$

where $\partial\Omega_{fs}$ and the normal vectors $\mathbf{n}_f$ and $\mathbf{n}_s$ are depicted in Fig. 1-A. In the fluid domain, mesh velocity $\mathbf{w}$ is derived following a Laplace smoothing method from the interface conditions.

2.4 Fluid and structural properties

In a viscous Newtonian incompressible fluid, the expression of the Cauchy stress tensor depends linearly on the strain rate:

$$\boldsymbol{\sigma}_f = -p\mathbf{I} + \eta_f (\nabla \mathbf{v}_f + {}^t\nabla \mathbf{v}_f) \ , \qquad (8)$$

with $\eta_f = 0.005\,\text{Pa.s}$ [42]. The first and second terms are respectively the hydrostatic component $\boldsymbol{\sigma}_f^{hydrostatic}$ and the viscous stress component $\boldsymbol{\sigma}_f^{viscous}$. The density of the fluid is set to $\rho_f = 1050\,\text{kg/m}^3$ [41].

Holzapfel et al. established a hyperelastic anisotropic constitutive equation for artery components [48]. This model is used here for each component of the plaque. Hyperelasticity implies the existence of a strain energy density function φ depending upon the Green-Cauchy right strain tensor $\mathbf{C}={}^t\mathbf{F}\mathbf{F}$, where $\mathbf{F}$ is the deformation gradient tensor [43]. Thus $\varphi = \varphi(\mathbf{C})$ and the associated Cauchy stress tensor is given by:

$$\boldsymbol{\sigma}_s = 2J^{-1}\mathbf{F}\frac{\partial \varphi}{\partial \mathbf{C}}{}^t\mathbf{F}, \qquad (9)$$

where $J = \det(\mathbf{F})$ is the volume change invariant. This formulation is valid for a solid without residual stresses. It was proposed in [48] to separate the isotropic and the anisotropic part of φ. The anisotropy is defined by two preferred directions corresponding to two families of collagen fibres. The angle between these two families of fibres is denoted β. $\mathbf{M} = \begin{pmatrix} 0 \\ \cos(\beta) \\ \sin(\beta) \end{pmatrix}$ and $\mathbf{M'} = \begin{pmatrix} 0 \\ \cos(\beta) \\ -\sin(\beta) \end{pmatrix}$ represent the directions of fibres in the local coordinate system.

Then, the strain energy density φ is written such as:

$$\varphi(I_1, I_4, I_6, J) = \frac{c}{2}(I_1 - 3) + \frac{k_1}{2k_2}\sum_{i=4,6}(e^{k_2(I_i-1)^2} - 1) + \frac{\kappa}{2}(J-1)^2, \qquad (10)$$

where $I_1 = tr(\mathbf{C})$, $I_4 = \mathbf{M}.(\mathbf{CM})$ and $I_6 = \mathbf{M'}.(\mathbf{CM'})$, c, κ, k_1 and k_2 are material parameters. Arterial tissue is often assumed as nearly incompressible [49]. The modulus of

compressibility κ is set to 500,000 kPa here in order to ensure this hypothesis. The density is set to $\rho_s = 900\,\mathrm{kg/m^3}$. Reference values of parameters c, k_1 and k_2 are given in Tab. 1. They were taken from experimental data [50].

To simplify the model, average properties of the media and of the adventitia reported in [50] are taken. For deducing the properties of the healthy artery reported in Tab. 1, a weighted average is derived, with a weight of $\frac{2}{3}$ for the media and a weight of $\frac{1}{3}$ for the adventitia [38]. The equation used to derive parameter *c* is given Eq. 11. A similar equation is used for the other mechanical parameters (k_1, k_2 and β).

$$c^{wall} = \frac{2}{3}c^{media} + \frac{1}{3}c^{adventitia} \qquad (11)$$

2.5 Numerical computation

FSI simulations are performed using commercial FE solver COMSOL Multiphysics [51]. The compatible finite-element types are P_2 for the fluid velocity $\mathbf{v}_f$, P_1 for the fluid pressure p and P_2 for the solid displacement $\mathbf{u}_s$ [52]. The model geometry is meshed using triangular mesh generation in COMSOL Multiphysics, consisting in N_f elements for the fluid domain ($2680 \le N_f \le 3316$) and N_s for the solid domain ($3476 \le N_s \le 4325$), with $N_{fibrous\ cap}$ elements in the thickness of the fibrous cap ($1025 \le N_{fibrous\ cap} \le 1650$), depending on the different model geometries considered in the parametric study. The coupled fluid-structure problem is discretized using a Galerkin-Least-Square method (GLS) and an implicit temporal discretization of order 5 using a Backward Differentiation Formula (BDF) with an adaptative time step. The non-linear problems are solved using a Newton-Raphson algorithm.

The mesh is refined close to the wall in order to take into account the viscous boundary layer: the mesh size is prescribed 3 times finer near the wall than at the centre.

The minimum and the maximum Reynolds number (Eq. 12) are respectively Re_{min}=300 and Re_{max}=2000. The value of Re_{max} justifies the use of a turbulence model [41]. The flow is modelled as being turbulent with the k-ω model [51].

$$\mathrm{Re} = \frac{\rho V D}{\mu}, \quad (12)$$

where D is the inner diameter of the artery and V is the axial velocity: for Re_{min}, D and V are taken at diastole in the healthy artery upstream the plaque and for Re_{max}, D and V are taken at systole at the top of the stenosis.

The geometry described in section 2.1 is the unloaded pressure-free geometry corresponding to the initial condition of the numerical computation. The simulation is performed over four cardiac cycles. During the first cardiac cycle, the pressurization and the average blood flow are applied before considering pulsatile effects. During this stage, the fluid viscosity, the pressure at the outlet and the velocity at the inlet are set gradually in order to ensure numerical convergence:

- the axial velocity at the inlet is increased linearly from 0m/s to 0.3m/s (see $v_z(t=0)$ Fig. 2-A)
- the pressure at the outlet is increased linearly from 0mmHg to 91mmHg (see $p(t=0)$ Fig. 2-B)
- the fluid viscosity is decreased linearly from 0.05Pa.s to 0.005Pa.s

Afterwards, three cycles of the actual pulsatile flow (see Fig. 2) are computed. The flow is fully established and periodic over the last cycle. Hence, the last cycle is used for the analysis.

2.6 Parametric study

In our model, different plaque parameters are set for reproducing the variability of real plaques:

- the fibrous cap thickness denoted *e*,
- material parameter k_1 in the arterial wall and in the fibrous cap, respectively denoted k_1^{wall} and k_1^{cap},
- stenosis severity *S* defined in Eq. 1
- stenosis length *L*.

Each parameter is set independently of the other parameters (unidirectional parametric study). The geometrical properties of the reference model are: $e = 0.1\text{mm}$, $S = 45\%$, $L = 10\,\text{mm}$. The reference values for k_1 are reported in Tab. 1. Simulations and analysis are performed for a wide range of these parameters using an interface between the COMSOL software and the MATLAB software [51,53].

The current study considers moderately severe plaques, between 20% and 70%. The current study is more focused on the effect of the stenosis length, as the effect of this parameter is not clearly understood and there exists a large range of plaque lengths. Plaques in the carotid artery may be short (*L*<10mm) [18,40]. Therefore, plaque lengths ranging between 5mm and 20mm are considered in this study (20 mm corresponds to a very long plaque [40]).

373 The fibrous cap thickness and the material parameters are taken into account for investigating
374 the effect of the plaque stiffness.
375
376 **2.7 Analysed criteria**
377
378 The analysis is focused on the response at the systole. A special attention is paid to the four
379 following criteria:
380 • the maximum von Mises equivalent stress in the fibrous cap defined as,
381 $$\sigma_{\max}^{VM} = Max(\sigma^{VM}) = Max(\sqrt{\sigma_1^2 + \sigma_2^2 - \sigma_1\sigma_2}), \qquad (13)$$
382 where σ_1 and σ_2 are the principal stresses in the radial and longitudinal directions
383 • the maximum wall shear stress (WSS),
384 $$\tau_{\max} = Max(\left\|\boldsymbol{\sigma}_f^{viscous}\mathbf{n}_f\right\|) \qquad (14)$$
385 • the average radial strain of the plaque,
386 $$\varepsilon_R = \frac{U_R}{H_0 + h_0 + e + R_m}, \qquad (14)$$
387 where U_R is the radial displacement of the fibrous cap at the middle of the stenosis,
388 • the global shear strain of the plaque,
389 $$\gamma = \frac{U_z}{H_0 + h_0 + e + R_m}, \qquad (16)$$
390 where U_z is the longitudinal displacement of the fibrous cap at the middle of the
391 stenosis.
392

393 The maximum von Mises equivalent stress, $\sigma_{\max}^{VM}$, defined in Eq. 13, is chosen to reflect the
394 vulnerability of the plaque. The maximum WSS, $\tau_{\max}$, is mostly associated with the
395 formation, growth and remodelling of the plaque [19-21,54].
396
397 Criteria γ and ε_R give an indication about the deformability of the plaque. The larger γ, the
398 more deformable the plaque by shear. This mode of deformation is mostly induced by the
399 drag force of the flow. The larger ε_R, the more deformable the plaque in compression. This
400 mode of deformation is mostly induced by the pressure variations.
401
402 **2.8 Convergence study**
403
404 The four criteria presented in section 2.7 are used for assessing the convergence of the
405 numerical resolution.
406
407 Temporal convergence is obtained using an adaptative time step, with a maximal value of
408 0.001s. It was checked that the four criteria remain unchanged by decreasing the maximum
409 value of the time step.
410
411 The spatial convergence is obtained using over 2680 P_2P_1 elements for the fluid domain and
412 over 3476 P_2 elements for the solid domain. It has been checked that increasing the degree of
413 the shape functions to P_3 for the fluid velocity, P_2 for the fluid pressure and P_3 for the solid
414 displacement has only a marginal influence on the analysed criteria (Tab. 2).
415
416

3. Results

3.1. Response of the stenosed artery

An example of results obtained from a FE analysis is shown in Fig. 3. Fig. 3-A shows the distribution of the von Mises equivalent stress in the plaque and in the healthy artery upstream and downstream the plaque, using a colour-coded representation plotted onto the deformed geometry at the systole. For visualizing the deformation between diastole and systole, the shape of the stenosed artery at diastole is represented in grey.

The percentage of diameter change between diastole and systole is about 5% in the healthy part of the artery (Fig. 3-A2), which corresponds to physiological conditions measured using MRI [46]. The percentage of diameter change is smaller in the stenosed region, due to the stiffening effect of the wall thickening (Fig. 3-A2).

The longitudinal component of the velocity $v_z = \mathbf{v}_f \mathbf{.e}_z$ is also represented at systole in Fig. 3-B using a colour-coded representation. Due to Venturi effect, the velocity increases from about 0.5m/s upstream the stenosis to about 1.7m/s downstream the stenosis. Recirculation occurs downstream the stenosis.

In the next sections, the results of the parametric study are presented. In Fig. 4 and 5, the influence of parameters e, k_1^{wall} and k_1^{cap}, S, L, onto $\sigma_{\max}^{VM}$, $\tau_{\max}$, ε_R and γ is displayed.

3.2. Influence of the fibrous cap thickness.

441 The influence of the fibrous cap thickness *e* onto the mechanical criteria is studied. For that,
442 parameters (*S*,*L*) are set to (45%,10mm) and k_1^{wall} and k_1^{cap} are set to the values reported in
443 Tab. 1. The increase of $\sigma_{\max}^{VM}$ with respect to the decrease of the fibrous cap thickness *e*,
444 shown in Fig. 4-A1, is in agreement with other studies stating that a thin fibrous cap is the
445 parameter mostly associated with the plaque vulnerability [15,23]. The increase of $\sigma_{\max}^{VM}$ is
446 more important from *e*=0.1mm to *e*=0.05mm. This result can be related to the result of Li et
447 al. [15]. They showed that $e \le 0.1mm$ could result in plaque rupture, even for a small stenosis
448 severity.
449
450 The ratio between the volume of the lipid core and the fibrous cap thickness is sometimes
451 used to characterise the plaque vulnerability: the greater this ratio, the more vulnerable the
452 plaque [55] but Gao and Long [27] showed that the stress level in the fibrous cap is more
453 sensitive to the fibrous cap thickness than to the lipid core volume.
454
455 Moreover as shown in Fig. 4, when *e* decreases, the average compression strain ε_R decreases,
456 whereas the average shear strain γ and the maximal WSS $\tau_{\max}$ increases.
457
458 The stress criteria $\sigma_{\max}^{VM}$ and $\tau_{\max}$ and the deformation criteria ε_R and γ will be analysed in the
459 discussion considering a thin and homogenous fibrous cap (*e*=0.1mm).
460
461 **3.3 Influence of the stiffness of the constituents.**
462
463 The influence of the material parameters k_1^{wall} and k_1^{cap} onto the mechanical criteria are
464 studied considering that the other parameters are set to (*e*,*S*,*L*)=(0.1mm,45%,10mm). These

parameters are increased in the following range of values (in kPa): $24.53 \le k_1^{wall} \le 300$ and $23.7 \le k_1^{cap} \le 300$.

The variations of $\sigma_{\max}^{VM}$ with respect to k_1^{wall} and k_1^{cap} (Fig. 4-A2,A3) shows that the plaque is more stable when each of these parameters increases. This result is in agreement with other studies reporting that a calcified plaque (stiffer) is more stable. Moreover Imoto et al [56] showed that a calcified inclusion in the fibrous cap can stabilize the plaque. However, Vengrenyuk et al. [57] showed that a fibrous cap with micro-calcification inclusions is related with high stress concentration and plaque fracture. This means that local and small inclusions may have the opposite effect of large calcifications.

The effect of k_1^{wall} and k_1^{cap} on the other parameters (compression strain ε_R and average shear strain γ) is marginal within the range of tested values. Moreover, the mechanical properties of the healthy part of the artery affect only slightly the maximal WSS $\tau_{\max}$, whereas the mechanical properties of the fibre cap on the WSS is more pronounced. The decrease of $\tau_{\max}$ with regard to an increase of k_1^{cap} is interesting; it shows that a compliant plaque is more prone to local erosion by wall shear stress. The behaviour of a compliant plaque, using the material parameters given in Tab. 1 [50], onto the stress and deformation criteria will be detailed in the discussion.

3.4 Influence of the stenosis severity

The effects of the stenosis severity is investigated through the following range of values: 25%<*S*<70% with a constant plaque length *L*=10mm. The fibrous cap thickness is set to *e*=0.1mm and the values of k_1^{wall} and k_1^{cap} are reported in Tab. 1. In current clinical practice,

when a vulnerable plaque is subjected to triggering events, the degree of severity of endoluminal stenosis (Eq. 1) is evaluated and the plaque is diagnosed as vulnerable if this criterion is beyond 70% [5,6]. With our model, the mechanical response is analyzed within a range of stenosis severities which are below the vulnerability threshold. Fig. 5-A (left) shows that $\sigma_{\max}^{VM}$ is around 400kPa for $20\% \le S \le 45\%$ ($\sigma_{\max}^{VM}(20\%) = 404.53\,\text{kPa}$, $\sigma_{\max}^{VM}(35\%) = 413.19\,\text{kPa}$ and $\sigma_{\max}^{VM}(45\%) = 384.46\,\text{kPa}$) and increases to around 500kPa for *S*=55% ($\sigma_{\max}^{VM}(55\%) = 540.31\,\text{kPa}$) and to around 600kPa for *S*=70% ($\sigma_{\max}^{VM}(70\%)$ =627.80kPa) which confirms that the degree of endoluminal stenosis affects the plaque vulnerability.

3.5 Influence of the stenosis length

Moreover, Fig. 5-A (right) shows that the plaque length is also strongly related to the plaque vulnerability even though this criterion is not taken into account in clinical practice. For instance, on one hand, the plaque with the parameters (*S*,*L*)=(55%,10mm) has a similar $\sigma_{\max}^{VM}$ value as the plaque with the parameters (*S*,*L*)=(45%,5mm): $\sigma_{\max}^{VM}$ (55%,10mm)=540.31kPa and $\sigma_{\max}^{VM}$ (45%,5mm)=541.21kPa. On the other hand, for two plaques having the same severity *S*=45%, the maximum stress $\sigma_{\max}^{VM}$ is 50% larger in the short plaque (*L*=5mm) than in a larger plaque (*L*=10mm), and the maximum WSS $\tau_{\max}$ is increased of 100%.

In Fig. 5, it can be remarked that increasing the stenosis severity or decreasing the plaque length has similar effects on the mechanical criteria. The influence of both the stenosis severity and the plaque length on the fluid structure interaction and on the plaque vulnerability will be discussed in the next section.

4. Discussion

4.1 Compression or shear effects

In Fig. 5-C and D, the deformability of the plaque is investigated through its average compression strain ε_R and its average shear strain γ. Considering that the stenosis length is set to $L = 10mm$, in Fig. 5-C and D (left), it can be noted that the mode of deformation changes drastically between $S = 35\%$ and $S = 45\%$, inducing a transition. On one hand, below the transition, the compression strains overwhelm the shear strains. On the other hand, beyond the transition severity, the opposite effect occurs.

Increasing the stenosis severity or decreasing the plaque length has similar effects on the mechanical criteria. Considering that the stenosis severity is set to $S = 45\%$, in Fig. 5-C and D (right) it appears a transition zone between $L = 10\,\text{mm}$ and $L = 15\,\text{mm}$. Beyond the transition length, the compression strains overwhelm the shear strains, whereas the opposite effect occurs for short stenoses.

This transition is illustrated in Fig. 6-A which shows the stress distribution in the fibrous cap (σ^{VM}) for different severities and different lengths. It is noticeable that for $(S, L) = (35\%, 10\text{mm})$ or for $(S, L) = (45\%, 15\text{mm})$ the stress distribution is controlled by the blood pressure. In this case, high stresses are localized on the top of the stenosis. On the other hand, for (*S*,*L*)=(45%,10mm) or for (*S*,*L*)=(55%,10mm) or for (*S*,*L*)=(45%,5mm), the stress distribution is controlled shear which induces a localization of high stresses upstream stenosis.

If shear overwhelms compression, the plaque length has a significant effect onto the plaque vulnerability. The shorter the plaque, the more vulnerable.

If compression overwhelms shear, the study shows that a solid model without FSI, just considering pressure loads, is sufficient [23-26]. However, a model with FSI is necessary when the shear effects become significant [9,10,18,27-33]. This remark is interesting for choosing appropriate patient-specific models.

4.2 Plaque pinching

If shear overwhelms compression, results shown in Fig. 6-A give an interesting explanation for the deformed shape of the fibrous cap. Indeed, it can be observed that the plaque is compressed from both sides of the stenosis, upstream and downstream, resulting in a pinching effect of the plaque. The pinching effect comes from the coupled action of two phenomena:

- the shear coming from two flows:
    - the global flow upstream stenosis
    - the flow recirculation downstream stenosis
- the depression coming from:
    - the Venturi effect on the top of the stenosis
    - the recirculation downstream stenosis

Each flow compresses the stenosis on both sides, upstream and downstream. This phenomenon is schematized in Fig. 7-A. Due to the Venturi effect and flow recirculation, the pressure decreases [58], inducing outward tractions onto the plaque. These phenomena may also induce buckling in the fibrous cap.

In Fig. 7-B, the response of the plaque has been plotted by considering only the action of the blood pressure, without the action of blood flow. The results show that the mechanical response is completely different, without pinching effect.

The pinching effect appears for moderately thin fibrous cap (e=0.2mm) and increases when the fibrous cap thickness decreases. It is illustrated by the increase of the shear strain γ and the decrease of the compression strain ε_R with respect to the decrease of the fibrous cap thickness e, respectively shown in Fig. 4-C1 and D1.

As shown in Fig. 6-A, the plaque pinching does not present an upstream-downstream symmetry. For instance, for L=5mm and for S=55% (Fig. 6-A), there is no symmetry because the global flow, the flow recirculation and the recirculation depression do not produce the same magnitude of force acting upstream and downstream the stenosis.

This puts in evidence that the action of blood flow is essential because it induces stress concentrations. Tang et al. evoked already that a local stress concentration is more closely related to plaque fracture [9] but the pinching effect has never been referenced.

Localization of the WSS (τ) is also shown in Fig. 6-B, with high concentrations when the plaque is pinched. As WSS may be related with the plaque ulceration [19-21], the results show that when the pinching effect is strong, this may also induce plaque ulceration in real cases.

4.3 Main limitations

The mechanical properties of the artery. The Holzapfel material model was chosen because it is an appropriate model taking into account the nonlinear and anisotropic behaviour of arteries. Other material models could be used as Mooney-Rivlin models [28,59] and Ogden hyper-elastic models [13,15]. It has been verified that the pinching effect and the importance of plaque length are preserved even if these other material models are used. They are also preserved if different properties are considered for both layers of the healthy artery (media and adventitia, see section 2.4). Actually, as shown in Fig. 4-A2, B2, C2 and D2, the material properties of the healthy artery wall have a marginal influence on the pinching effect.

An important question is also the convexity of strain energy function defined in Eq. 10. As recommended by Holzapfel et al. [64], if I_4 and/or I_6 are less than 1, their contribution is cancelled from the strain energy function. This guarantees the convexity of the strain energy function whatever the material parameters.

Another important question is the impact of the choice of the material parameters of the artery on the mechanical response. The results displayed in Fig. 4 tend to show that the impact of the material properties of the artery onto the response of the plaque is less important than the impact of geometrical parameters like the severity, the thickness and the length.

However, the material properties of the artery used in the parametric study are defined as averages of the properties of the media and of the adventitia. It has been verified that this simplification does not alter the form of the mechanical response of the artery. For this verification, the longitudinal and circumferential stress/stretch curves of the different models of artery used in this paper have been plotted in Fig. 8 and compared to the stress/stretch curves of the original models taken from Gasser et al. [50]. It can be observed that the variety of parameters tested in our parametric study encompass the stress/stretch curves of the media and adventitia models reported in [50]. Moreover, the different curves have similar shapes,

612 which show that varying the parameters of the model results mainly in variations of the
613 compliance of the artery itself.
614
615 **The perivascular tissues.** The vessel receives perivascular constraint from the surrounding
616 tissues [60]. Considering the stiffness of the surrounding tissue may increase the rigidity of
617 the structure, similarly as playing with the stiffness of the artery wall itself. It has been
618 observed that the material properties of the healthy artery wall have a marginal influence on
619 the analysed mechanical criteria (Fig. 4-A2, B2, C2 and D2). Then the effect of the
620 surrounding tissue may not be considered as prominent.
621
622 **The blood viscosity.** Stenoses have an influence on the blood flow but can also have an
623 impact on its viscosity. The blood is not a Newtonian fluid. The blood, composed of 80%
624 plasma, may be assumed as a Newtonian fluid in healthy arteries with diameter larger than
625 5 mm. But the presence of red cells influences the blood viscosity when the hematocrite (ratio
626 between the volume of red cells and the volume of plasma) increases. It is the case when the
627 arterial lumen decreases or when the red cells aggregates [41,61]. This aggregation occurs in
628 an area with many red cells and where the shear stress is less than 1 Pa [62]. Such a zone can
629 be localized in a recirculation like downstream the stenosis. The red cells are trapped in a
630 zone where they can aggregate. This case should be taken into account if one would like to
631 refine the local shear stress just downstream the stenosis.
632
633 **The boundary conditions.** The effect of pressure and flow variability is not analysed. Such
634 analysis may be interesting with regard to the pinching effect and it will be achieved in the
635 future. Moreover, the existence of an axial pretension in the artery (tethering effect) is also an

aspect that may be important, especially concerning the zero-stress state in real geometries [32,63]. Given that our geometries were ideal, this aspect was not considered.

The geometry. This study offers an analysis of the influence of plaque shape on fluid structure interactions especially concerning the plaque length. Nevertheless there is no axisymmetric plaque in real case and the dimensions of the plaque used in our study are not representative of a given physiological scenario. The dimensions of the plaque were defined for encompassing a wide range of possible scenarii regarding plaque lengths, plaque severities, fibre cap thickness and material properties of the tissues. Other models are under development: asymmetric plaques, axisymmetric plaques with shape irregularities. The radius of the artery used in this study is based on the dimensions of the human common carotid artery [43,65]. It would also be interesting to evaluate the effect of the artery radius for mimicking for instance the plaque behaviour in the internal carotid artery which is smaller.

The unloaded state of the artery

The arterial radius for the unloaded (no pressure) condition was set at 3.00 mm and the average arterial radius for the pressurized condition (Fig. 3-A2) was 3.625 mm at diastole and 3.825 mm at systole. This indicates an expansion of artery. This expansion was not calibrated upon physiological data. It was applied because the hyperelastic constitutive equations are a model of the mechanical behaviour with regard to the unloaded (no pressure) state of the artery. However, we did not study how the choice of the unloaded geometry affects the mechanical response of the plaque. Moreover, the effect of the axial prestretch is also an aspect that still has to be evaluated.

5. Conclusion

This study shows that geometric and mechanical properties of atheromatous plaques affect significantly its mechanical response to the action of pulsatile blood flow. Notably for a short, severe and compliant stenosis, the blood pinches the plaque. In this case the stress localization and plaque vulnerability is emphasized.

These results may offer some new perspectives for understanding the vulnerability of short plaques. Unfortunately there are only few experimental papers available on this subject in the literature. Future work will consist in achieving such experimental investigations for characterizing the vulnerability of short plaques from clinical data. Moreover, more sophisticated models are under development in order to evaluate the effects of shape irregularities and asymmetry.

6. Conflict of interest

None.

7. Acknowledgements

This study is part of the Imandef project (Grant ANR-08-JCJC-0071) funded by the ANR (French National Research Agency).

References

[1] Rosamond W, Flegal K et al.. Heart Disease and Stroke Statistics - 2007 Update. A Report From the American Heart Association Statistics Committee and Stroke Statistics Subcommittee. Circulation 2007;115:69-171.

[2] Virmani R, Ladich E, Burke A, Kolodgie F. Histopathology of Carotid Atherosclerotic Disease. Neurosurgery 2006;59(5):219-227.

[3] Lipinsky MJ, Frias JC, Fayad HA. Advances in detection and characterization of atherosclerosis using contrast agent targeting the macrophage. Journal of Nuclear Cardiology 2006;13:699-609.

[4] Carr S, Farb A, Pearce WH, Virmani R, Yao JST. Atherosclerotic plaque rupture in symptomatic carotid artery stenosis. Journal of Vascular Surgery 1996;23:755-766.

[5] ECST, MRC European Carotid Surgery Trial. Interim results for symptomatic patients with severe (70%-99%) or with mild (0%-29%) carotid stenosis. European Carotid Surgery Trialists Collaborative Group. The Lancet 1991;337:1235-1243.

[6] NASCET. Beneficial effect of carotid endarterectomy in symptomatic patients with high grade stenosis. The New England Journal of Medecine 1991;325:445–453.

[7] Toussaint JF, LaMuraglia GM, Southern JF, Fuster V, Kantor HL. MR images of lipid, fibrous, calcified, hemorrhagic and thrombotic components of human atherosclerosis in vivo. Circulation 1996;94:932-938.

[8] Cai JM, Hatsukami TS, Ferguson MS, Small R, Polissar NL, Yuan C. Classification of human carotid atherosclerotic lesions with in vivo multicontrast magnetic resonance imaging. Circulation 2002;1006:1368-1373.

[9] Tang D, Yang C, Zeng J, Woodard PK, Saffitz JE, Petruccelli JD, Sicard GA, Yuan C. Local Maximal Stress Hypothesis and Computational Plaque Vulnerability Index for

710 Atherosclerotic Plaque Assessment. Annals of Biomedical Engineering 2005;33:1789–
711 1801.
712 [10] Tang D, Teng Z, Canton G, Yang C, Ferguson M, Huang X, Zheng J, Woodard PK,
713 Yuan C. Sites of Rupture in Human Atherosclerotic Carotid Plaques Are Associated
714 With High Structural Stresses. An In Vivo MRI-Based 3D Fluid-Structure Interaction
715 Study. Stroke 2009;40:3258-3263.
716 [11] Bank AJ, Versluis A, Dodge SM, Douglas WH. Atherosclerotic plaque rupture: a fatigue
717 process. Medical Hypotheses 2000;55(6):480-484.
718 [12] Tang D, Yang C, Walker H, Kobayashi S, Ku DN. Simulating cyclic artery compression
719 using a 3D unsteady model with fluid-structure interactions. Computers and structures
720 2002;80:1651-1665.
721 [13] Versluis A, Bank AJ, Douglas WH. Fatigue and plaque rupture in myocardial infarction.
722 Journal of Biomechanics 2006;39:339-347.
723 [14] Ohayon J, Finet G, Gharib AM, Herzka DA, Tracqui P, Heroux J, Rioufol G, Kotys MS,
724 Elagha A, Pettigrew RI. Necrotic core thickness and positive arterial remodeling index:
725 emergent biomechanical factors for evaluating the risk of plaque rupture. American
726 Journal of Physiology – Heart and Circulatory Physiology 2008;295:717-727.
727 [15] Li ZY, Howarth SPS, Tang T, Gillard JH. How critical is fibrous cap thickness to carotid
728 plaque stability? A flow-plaque interaction model. Simulation of the interaction between
729 blood flow and atherosclerotic plaque. Stroke 2006;37:1195-1199.
730 [16] Li MX, Beech-Brandt JJ, John LR, Hoskins PR, Easson WJ. Numerical Analysis of
731 pulsatile blood flow and vessel wall mechanics in different degrees of stenoses. Journal
732 of Biomechanics 2007;40:3715-3724.

733 [17] Tang D, Yang C, Ku DN. A 3-D thin wall model with fluid-structure interactions for
734 blood flow in carotid arteries with symmetric and asymmetric stenoses. Computers and
735 structures 1999;72:357-377.
736 [18] Tang D, Woodard PK, Zeng J, Huang X, Yang C, Ferguson M, Yuan C, Canton G, Teng
737 Z. 3D Critical Plaque Wall Stress Is a Better Predictor of Carotid Plaque Rupture Sites
738 Than Flow Shear Stress: An In Vivo MRI-Based 3D FSI Study. Journal of
739 Biomechanical Engineering 2010;132:031007-1-9.
740 [19] Groen HC, Gilsen FJH, van der Lugt A, Ferguson MS, Hatsukami TS, van der Stenn
741 AFW, Yuan C, Wentzel JJ. Plaque fracture in carotid artery is localized at the high shear
742 stress region: A case report. Stroke 2007;38:2379-2381.
743 [20] Cheng C, Tempel D, van Haperen R, van der Baan A, Grosveld F, Daemen MJAP,
744 Krams R, de Crom R. Atherosclerotic lesion size and vulnerability are determined by
745 patterns of fluid shear stress. Circulation 2006;113:2744-2753.
746 [21] Fukumoto Y, Hiro T, Yamada J, Okamura T, Matsuzaki M. Localized elevation of shear
747 stress is related to coronary plaque rupture: a 3-dimensional intravascular ultrasound
748 study with in vivo color mapping of shear stress distribution. Journal of American
749 College of Cardiology 2008;51(6):645-650.
750 [22] Richardson PD, Davies MJ, Born GVR. Influence of plaque configuration and stress
751 distribution on fissuring coronary atherosclerotic plaques. The Lancet 1989;334:941-
752 944.
753 [23] Loree HM, Kamm RD, Stringfellow RG, Lee RT. Effects of Fibrous Cap Thickness on
754 Peak Circumferential Stress in Model Atherosclerotic Vessels. Circulation Research
755 1992;71:850-858.

[24] Ohayon J, Teppaz P, Finet G, Rioufol G. *In vivo* prediction of human coronary plaque rupture location using intravascular ultrasound and the finite element method. Coronary Artery Disease 2001;12:655-663.

[25] Ohayon J, Finet G, Treyve F, Rioufol G, Dubreuil O. A three-dimensional finite element analysis of stress distribution in a coronary atherosclerotic plaque: *In-vivo* location of plaque rupture location. Biomechanics applied to Computer Assisted Surgery 2005:225-241.

[26] Li ZY, Howarth S, Trivedi R, Kim-Im JMU, Graves MJ, Brown A, Wang L, Gillard JH. Stress analysis of carotid plaque fracture based on in vivo high resolution MRI. Journal of Biomechanics 2006;39:2611-2622.

[27] Gao H, Long Q. Effects of varied lipid core volume and fibrous cap thickness on stress distribution in carotid arterial plaques. Journal of Biomechanics 2008;41:3053–3059.

[28] Tang D, Yang C, Zheng J, Woodard PK, Sicard GA, Saffitz JE, Yuan C. 3D MRI-Based Multicomponent FSI Models for Atherosclerotic Plaques. Annals of Biomedical Engineering 2004;32(7):947-960.

[29] Yang C, Tang D, Yuan C, Hatsukami TS, Zheng J, Woodard PK. In Vivo/Ex Vivo MRI-based 3D Non-Newtonian FSI Models for Human Ahterosclerotic Plaques Compared with Fluid/Wall-Only Models. National Institutes of Health Public Access 2007;19(3):233-246.

[30] Kock SA, Nygaard JV, Eldrup N, Fründ ET, Klaerke A, Paaske WP, Falk E, Yong Kim W. Mechanical stresses in carotid plaques using MRI-based fluid–structure interaction models. Journal of Biomechanics 2008;41:1651-1658.

[31] Leach JR, Rayz VL, Soares B, Wintermark M, Mofrad M, Saloner D. Annals of Biomedical Egineering 2010;38(8):2748-2765.

780 [32] Huang X, Yang C, Yuan C, Liu F, Canton G, Zheng J, Woodard PK, Sicard GA, Tang D.
781 Patient-specific artery shrinkage and 3D zero-stress state in multi-component 3D FSI
782 models for carotid atherosclerotic plaques based on in vivo MRI data. Molecular and
783 Cellular Biomechanics. 2009Jun;6(2):121-34.
784 [33] Gao H, Long Q, Das KS, Halls J, Graves M, Gillard JH, Li ZY. Study of carotid arterial
785 plaque stress for symptomatic and asymptomatic patients. Journal of Biomechanics
786 2011;44:2551-2557.
787 [34] Valencia A, Baeza F. Numerical simulation of fluid-structure interaction in stenotic
788 arteries considering two layer nonlinear anisotropic structural model. International
789 Communications in Heat and Mass Transfer 2009;36:137-142.
790 [35] Tang D, Yang C, Huang Y, Ku DN. Wall stress and strain analysis using a three-
791 dimensional thick wall model with fluid structure interactions for blood flow in carotid
792 arteries with stenoses. Computers and structures 1999;72:341-356.
793 [36] Tang D, Yang C, Kobayashi S, Zheng J, Vito RP. Effect of Stenosis Asymmetry on
794 Blood Flow and Artery Compression: A There-Dimensional Fluid-Structure Interaction
795 Model. Annals of Biomedical Engineering 2003;31:1182-1193.
796 [37] Konala BC, Das A, Baneriee RK. Influence of arterial wall compliance on the pressure
797 drop across coronary artery stenoses under hyperemic flow condition. Mol Cell
798 Biomech. 2011; 8(1):1-20.
799 [38] Fung YC. Biomechanics: Mechanical Properties of Living Tissues. Second Edition.
800 Springer-Verlag NY Inc.. 1993.
801 [39] Miura T, Matsukawa N, Sakurai K, Katano H, Ueki Y, Okita K, Yamada K, Ojika K.
802 Plaque Vulnerability in Internal Carotid Arteries with Positive Remodeling.
803 Cerebrovascular Diseases Extra 2011;1:54-65.

[40] Douglas AF, Christopher S, Amankulor N, Din R, Poullis M, Amin-Hanjani S, Ghogawala Z. Extracranial Carotid Plaque Length and Parent Vessel Diameter Significantly Affect Baseline Ipsilateral Intracranial Blood Flow. Neurosurgery 2011Oct;69(4):767-73.

[41] Fung YC. Biomechanics, Circulation. Second Edition. Springer-Verlag NY Inc.. 1996.

[42] Formaggia L, Quarteroni A, Veneziani A. Cardiovascular Mathematics, Modelling and Simulation of the circulatory system. Volume 1. Springer. 2009.

[43] Fung YC, Tang P. Classical and computational solid mechanics. Volume 1. World Scientific. 2001.

[44] Uchida S. The Pulsating Viscous Flow Superposed on the Steady Laminar Motion of Incompressible Fluid in a Circular Pipe. ZAMP 1956;7(5):403-422.

[45] He X, Ku DN, Moore JE. Simple calculation of the velocity profiles for pulsatile flow in a blood vessel using Mathematica. Annals of Biomedical Engineering 1993;21(1):45-49.

[46] Avril S, Huntley JM, Cusack R. In vivo measurements of blood viscosity and wall stiffness in the carotid using PC-MRI. European Journal of computational Mechanics 2009;18:9-20.

[47] Masson I, Boutouyrie P, Laurent S, Humphrey JD, Zidi M. Characterization of arterial wall mechanical behavior and stresses from human clinical data. Journal of Biomechanics 2008;41:2618–2627.

[48] Holzapfel GA, Gasser TC. A New Constitutive Framework for Arterial Wall Mechanics and a Comparative Study of Material Models. Journal of Elasticity 2000;61:1-48.

[49] Carew TE, Vaishnav RN, Patel DJ. Compressibility of the arterial wall. Circulation Research 1968;23:63-68.

828 [50] Gasser TC, Holzapfel GA. Modelling Plaque Fissuring and Dissection during Balloon
829 Angioplasty Intervention. Annals of Biomedical Engineering2007;35(5):711-723.
830 [51] COMSOL MULTIPHYSICS 3.4: Fluid-Structure Interaction Module. COMSOL-AB,
831 Stockholm, Sweden.
832 [52] Zienkiewicz OC, Taylor RL. The Finite Element Method. Fifth Edition. Butterworth
833 Heineman. 2002.
834 [53] MATLAB R2007a. The MathWorks Inc, Natick, USA.
835 [54] Yang C, Canton G, Yuan C, Ferguson M, Hatsukami TS, Tang D. Advanced human
836 carotid plaque progression correlates positively with flow shear stress using follow-up
837 scan data: An in-vivo MRI multi-patient 3D FSI study. Journal of Biomechanics
838 2010;43(13):2530-2538.
839 [55] Oppenheim C, Touzé E, Leclerc X, Schmitt E, Bonneville F, Vandermarcq P, Gerardin
840 E, Toussaint JF, Mas JL, Méder JF. IRM Haute résolution de l'athérosclérose
841 carotidienne: au-delà de la lumière artérielle. Journal de radiology 2008;89 :293-301.
842 [56] Imoto K, Hiro T, Fujii T, Murashige A, Fukumoto Y, Hashimoto G, Okamura T,
843 Yamada J, Mori K, Matsuzaki M. Longitudinal Structural Determinants of
844 Atherosclerotic Plaque Vulnerability. Journal of the American College of Cardiology
845 2005;46:735-1097.
846 [57] Vengrenyuk Y, Calier S, Xanthos S, Cardoso L, Ganaotos P, Virmani R, Einav S,
847 Gilchrist L, Weinbaum S. A Hypothesis of Vulnerable Plaque Fracture due to Stress-
848 Induced Debonding Around Cellular Microcalcifications in Thin Fibrous Cap.
849 Proceedings of the National Academy of Science 2006;103:14678-14683.
850 [58] Landau LD, Lifshitz EM. Fluid Mechanics. Second Edition. Volume 6. Butterworth
851 Heineman. 1987.

852 [59] Chau AH, Chan RC, Shishkow M, MacNeill B, Iftimia N, Tearney GJ, Kamm RD,
853 Bouma BE, Kaazempur-Mofrad MR. Mechanical Analysis of Atherosclerosclerotic
854 Plaques Based on Optical Coherence Tomography. Annals of Biomedical Engineering
855 2004;32(11):1494-1503.
856 [60] Tovar-Lopez F, Rosengarten G, Khoshmanesh K, Westein E, Jackson SP, Nesbitt WS,
857 Mitchell A. Structural ans hydrodynamic simulation of an acute stenosis-dependent
858 thrombosis model in mice. Journal of Biomechanics 2011;44(6):1031-1039.
859 [61] Owens R. A new microstructure-based constitutive model for human blood. Journal of
860 non-Newtonian Fluid Mechanics 2006;140:57-70.
861 [62] Mazumdar JN. Biofluid Mechanics. World Scientific. 2004.
862 [63] Lu J, Zhou X, Raghavan ML. Inverse elastostatic stress analysis in pre-deformed
863 biological structures: Demonstration using abdominal aortic aneurysms. Journal of
864 Biomechanics, 2007;40:693–696.
865 [64] Holzapfel GA, Gasser TC, Ogden RW. A new constitutive framework for arterial wall
866 mechanics and a comparative study of material models. Journal of Elasticity,
867 2000;61:1–48.
868 [65] Krejza J, Arkuszewski M, Kasner SE, Weigele J, Ustymowicz A, Hurst RW, Cucchiara
869 BL, Messe SR. Carotid Artery Diameter in Men and Women and the Relation to Body
870 and Neck Size. Stroke, 2006;37:1103-1105.
871
872

List of figures and table with caption:

Tab. 1: Material and structural parameters of the Holzapfel model describing the atheromatous plaque components.

Tab. 2: Spatial convergence: Values of the analysed criteria (see section 2.7) with the degree of shape functions used in the study (P_2 for $\mathbf{v}_f$, P_1 for p and P_2 for $\mathbf{u}_s$) and after increasing the degree of the shape functions (P_3 for $\mathbf{v}_f$, P_2 for p and P_3 for $\mathbf{u}_s$).

Tab. 3: Fourier coefficients for the velocity and pressure data.

Fig. 1: Schematic of the model geometry: (A) Domains, boundaries and vector orientation definition. (B) Schematic of the plaque components. (C) Geometric parameters. (D) 3-D representation.

Fig. 2: Curve of the axial velocity at the inlet (a) and of the pressure at the outlet (b) during a cardiac cycle.

Fig. 3: (A) Distribution of the von Mises equivalent stress in the plaque and in the healthy artery upstream and downstream the plaque (σ^{VM}), using a colour-coded representation on the deformed shape at systole. It is super-imposed to the shape at diastole, represented in grey. (A1) Zoom to the top of the stenosis. (A2) Variation of diameter vs. time over a cardiac cycle for native and stenosed regions of the arteries. (B) Distribution of the longitudinal component of velocity v_z represented at systole using a colour-coded representation.

Fig. 4: Influence of the fibrous cap thickness *e* and of material parameters k_1^{wall} and k_1^{cap} onto: (A) the maximum von Mises equivalent stress in the fibrous cap $\sigma_{\max}^{VM}$. (B) the wall shear stress (WSS) on the plaque $\tau_{\max}$. (C) the average radial strain of the plaque ε_R. (D) the average shear strain of the plaque γ. The stenosis severity and the stenosis length are respectively set to *S*=45% and *L*=10mm.

Fig. 5: Influence of the stenosis severity *S* and the stenosis length *L* onto: (A) the maximum von Mises equivalent stress in the fibrous cap $\sigma_{\max}^{VM}$. (B) the wall shear stress (WSS) on the plaque $\tau_{\max}$. (C) the average radial strain of the plaque ε_R. (D) the average shear strain of the plaque γ. On the left hand side, the stenosis length is set to *L*=10mm and on the right hand side, the stenosis severity is set to *S*=45%.

Fig. 6: Mode of deformation and vulnerability of the plaque with respect to stenosis severities *S* and lengths *L*: (A) Distribution of the von Mises equivalent stress in the fibrous cap (σ^{VM}), using a colour-coded representation. The shape at diastole is represented in grey and the stress distribution is represented on the deformed shape at systole. (B) WSS distribution in the fibrous cap (τ) using a colour-coded representation on the deformed shape at systole with velocity vectors.

Fig. 7: Interactions between the blood and the plaque with flow (A) and without flow (B) for parameters (*S*,*L*)=(45%,10mm): Schematic representation of the plaque deformed by the pinching effect (A1) and of the plaque deformed by compression without pinching effect (B1). Pressure distribution around the stenosis using a colour-coded representation (A2) and

922 (B2). Von Mises equivalent stress distribution in the fibrous cap (σ^{VM}), using a colour-coded
923 representation (A3) and (B3).
924
925 Fig. 8: Circumferential (a) and longitudinal (b) stress/stretch curves of the healthy artery
926 model for different material properties tested in the parametric studies and comparison with
927 the stress/stretch curves of the media and adventitia reported in [50].
928

929 Tab. 1

930

Components	c (kPa)	k_1 (kPa)	k_2 (-)	β (°)
Fibrous cap	78.9	23.7	26.3	0
Healthy artery wall	10.58	24.53	22.13	21
Lipid pool	0.1	0.0	-	-

931

932

933 Tab. 2

934

Finite elements types	$\sigma_{\max}^{VM}$ (kPa)	$\tau_{\max}$ (Pa)	ε_R	γ
P_2 for $\mathbf{v}_f$, P_1 for p and P_2 for $\mathbf{u}_s$	384.46	43.254	0.141	0.119
P_3 for $\mathbf{v}_f$, P_2 for p and P_3 for $\mathbf{u}_s$	384.46	43.312	0.139	0.122

935

936

937 Tab 3

k	v_k (cm/s)	p_k (mmHg)
0	27,8117	93.743
1	-0,1229-11,0224i	-2.4929-12.407i
2	-2,3484+8,5141i	-4.5547-3.3544i
3	5,8539-2,0908i	-2.5546-0.32889i
4	-2,9313-1,1926i	-0.6181+0.45323i
5	1,3812+2,1390i	-0.19113-0.26335i
6	0,7306-0,9195i	-0.79729-0.68989i
7		-0.88357+0.1032i
8		-0.25735+0.22093i
9		-0.37814-0.015991i
10		-0.36849+0.32603i
11		0.015548+0.22243i
12		-0.070833+0.058148i
13		-0.068578+0.13458i
14		0.040223+0.12718i
15		0.030337+0.028246i
16		-0.0060027+0.02907i
17		0.0054199+0.046419i
18		0.0053679+0.0085823i

938

939

940 Fig. 1

941

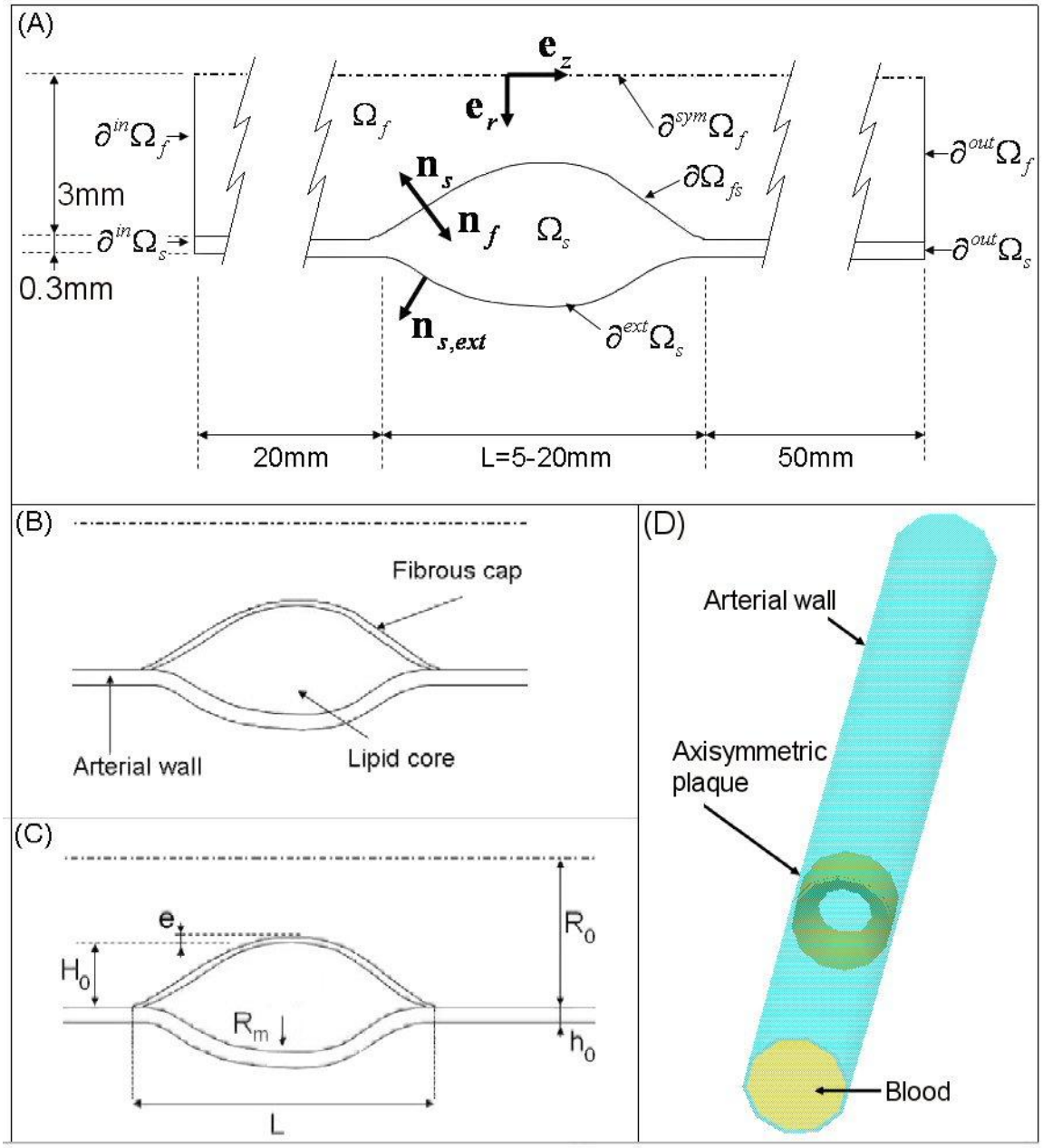

942

943

944 Fig. 2

945

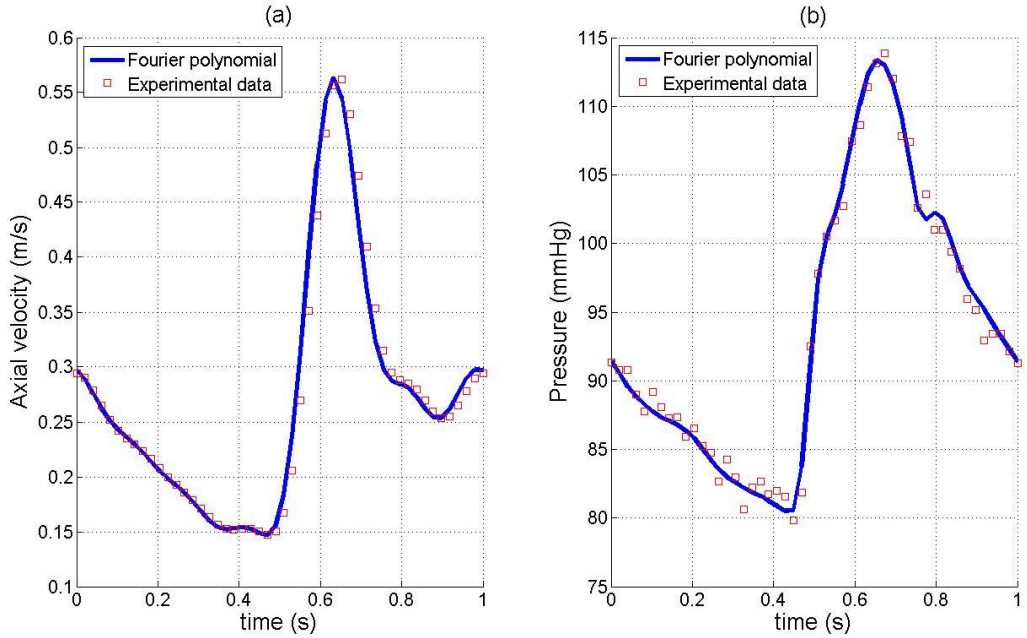

946

947

948 Fig. 3

949

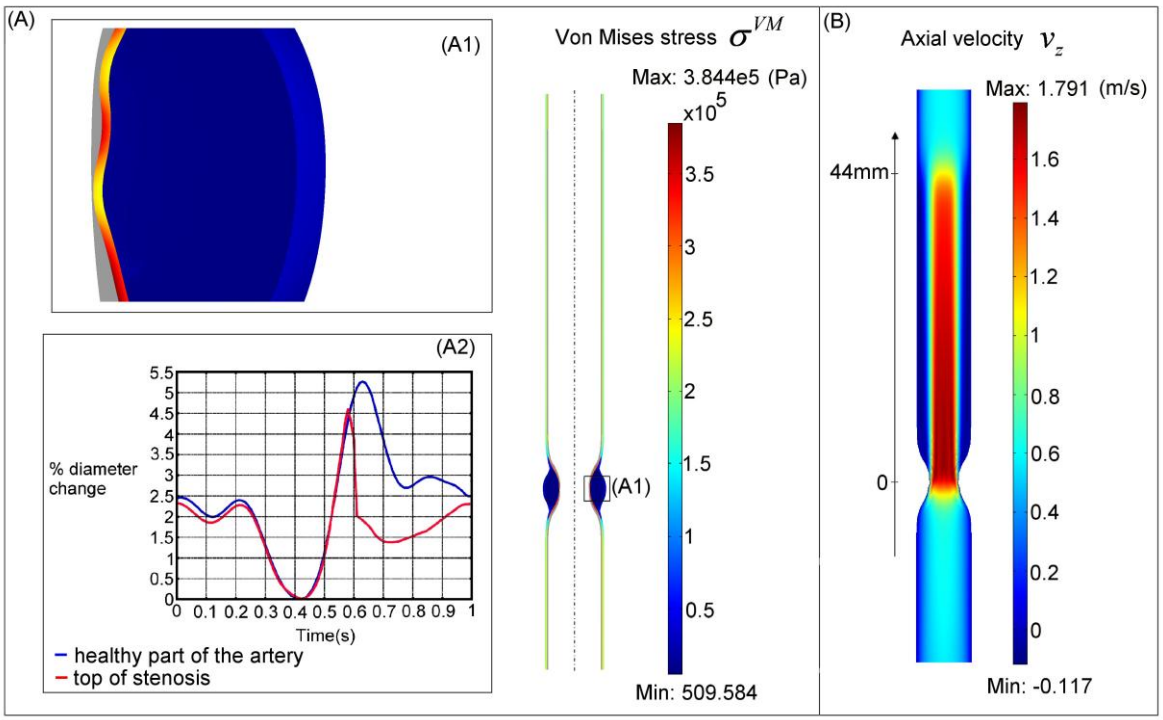

950

951

952 Fig. 4

953

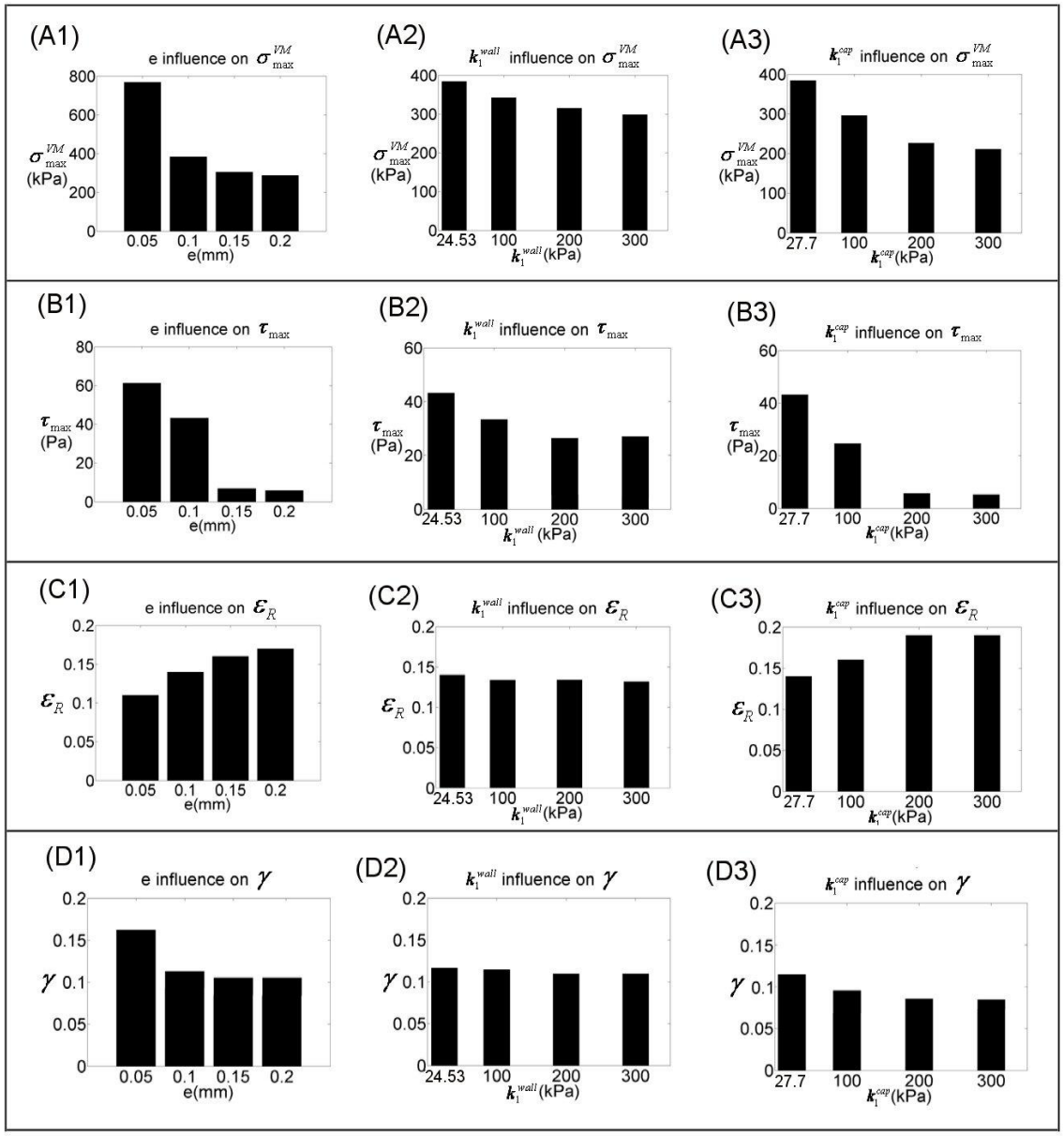

954

955

956 Fig. 5

957

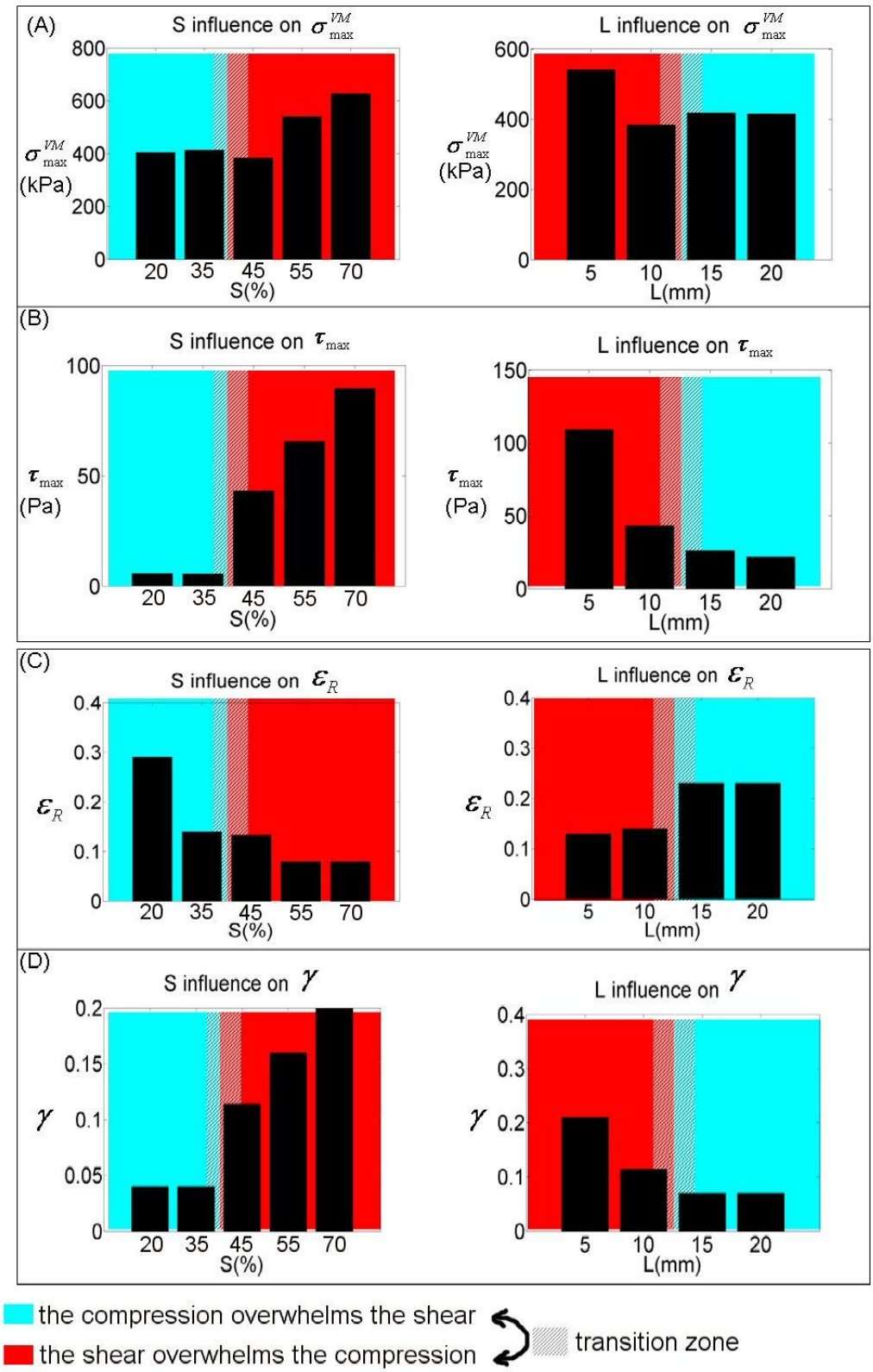

958

959

960 Fig. 6

961

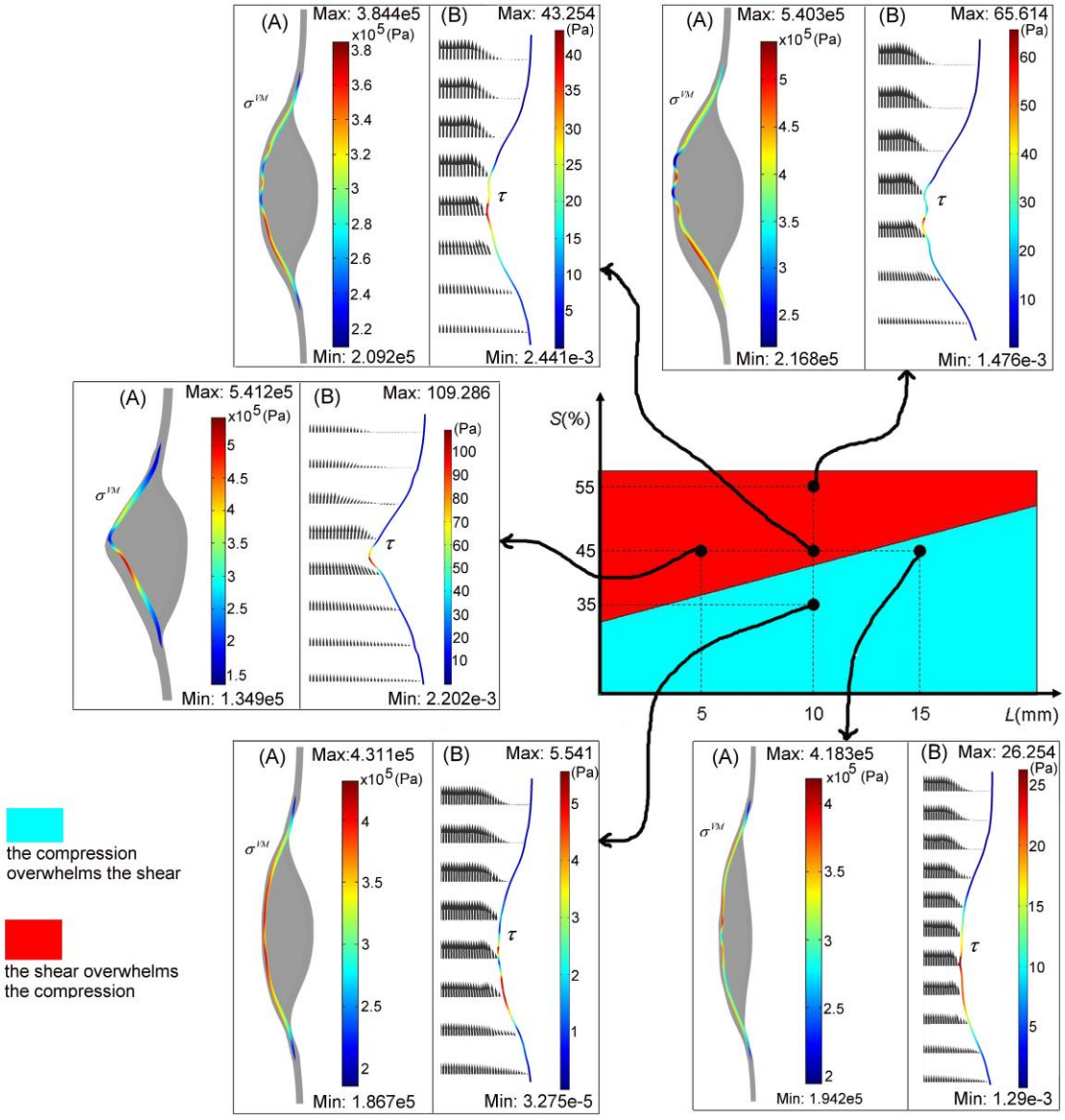

962

963

964 Fig. 7

965

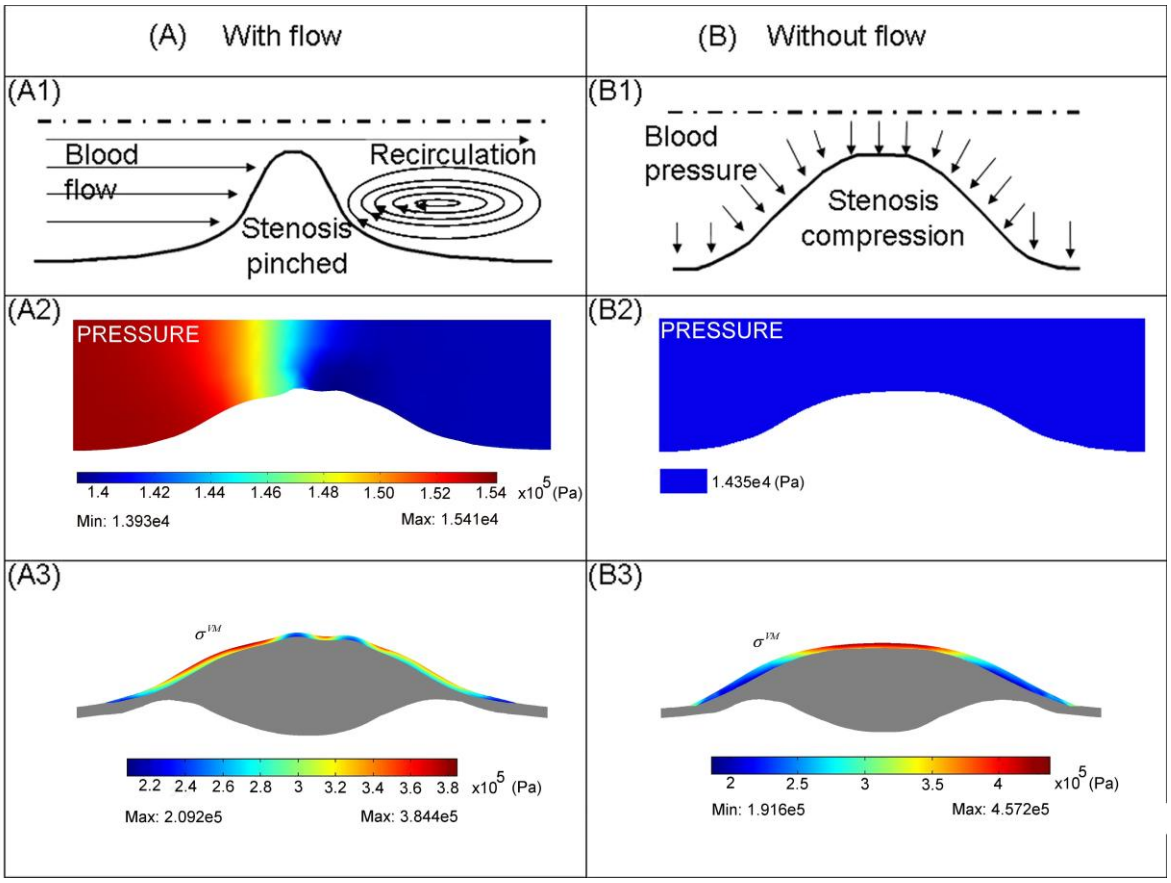

966

967

968 Fig 8

969

970

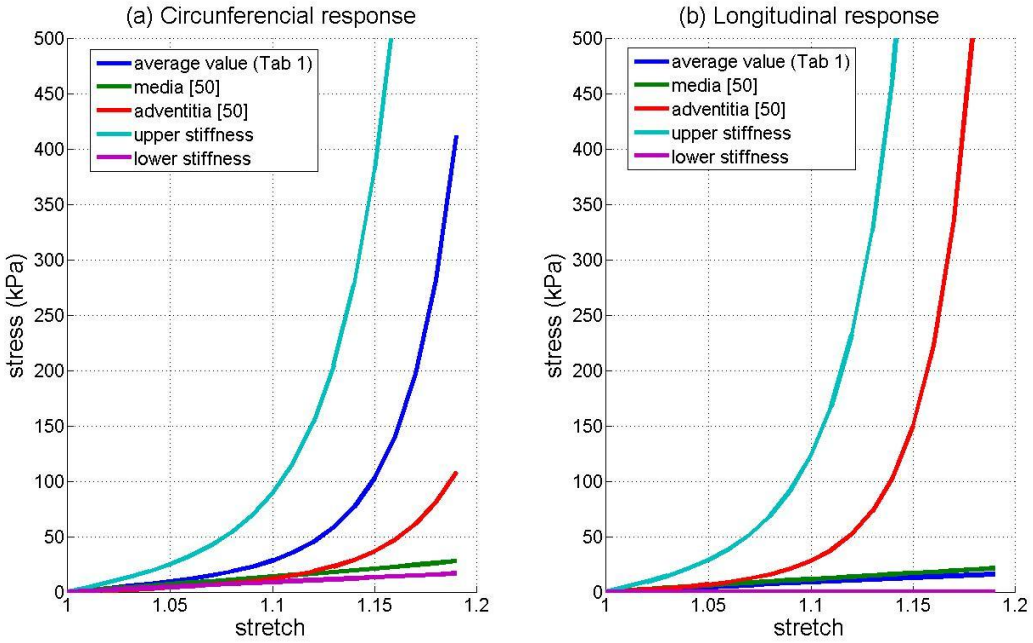

971